

Segmentation of Blood Vessels in Subtraction Angiographic Images

Martin Franz and Rene Schüffny

Stiftungsprofessur für Hochparallele VLSI-Systeme und Neuromikroelektronik,
Institut für Grundlagen der Elektrotechnik und Elektronik, Fakultät Elektrotechnik,
Technische Universität Dresden, Mommsenstr. 13, 01062 Dresden, Germany

Email: {franz,schueffn}@iee.et.tu-dresden.de

WWW: <http://www.iee.et.tu-dresden.de/iee/hpsn/>

Abstract. Digital radiology leads to a growing amount of medical images which impose severe demands on networking and storage resources. These requirements can be met using content-orientated image compression which reduces the amount of data while preserving the diagnostic information. This paper presents a new method for automated vessel segmentation which can be used for both, decision support systems and content-orientated image compression of angiograms.

1 Introduction

In 1995, the radiology department of a 1500-bed university hospital was already generating 20 Tbytes of image data per year [1]. Hence, electronic access and storage of radiology images is limited by storage capacities and network bandwidth. Content-orientated image compression can improve performance of picture archiving systems (PACS) while preserving the diagnostic information. This task is addressed by local adjustment of image quality for a given segmentation of foreground objects. However, segmentation is a very crucial problem. We propose new methods to perform an automated segmentation of blood vessels in digital subtraction angiograms (see figure 1). Segmentation can be used for both, clinical decision-making and content-orientated (semantic) image compression. Segmenting angiographic images is a very difficult task due to acquisition noise, vessel shape variability and tissue inhomogeneity. The best strategy to cope with these difficulties is exploiting as much as possible a-priori information about vessel structures. However, there does not exist a unique vascular model, which contains all the well-known blood vessel characteristics like

- local continuity of vessel position, curvature, diameter and density [2],
- graph structure, branching, connectivity and
- biological shape variability.

The application of top-down methods is not appropriate due to the high biological variability. Therefore, all investigated vessel recognition methods are bottom-up consisting of several consecutive stages with increasing semantic level, which process each of the vessel properties.



Fig. 1. Digital Subtraction Angiogram (DSA)

A lot of approaches for vasculature detection use differentiating operators to discover the vessel location. Well-known representatives are scale space methods [3], morphologic operators (dilatation gradient), and snakes. Obviously, vessels exhibit a contrast to the background and can be found in this way. However, problematic is the high noise sensitivity of differentiating operators, which results in a very uncertain recognition due to naturally high background noise in digital subtraction angiograms.¹ This disadvantage can be reduced by smoothing the image, but on the cost of information loss. More sophisticated smoothing algorithms use anisotropic diffusion where large gradients are preserved [4], but noise sensitivity of gradients makes the smoothing itself inaccurate. So we decided to avoid the application of differentiating operators.

Other methods use histograms [5], i.e. threshold values in the greyvalue interval are used to separate vessel and background. Most of the (especially long-term) knowledge about vessel geometry is ignored and so the segmentation result is poor. Hence, this approach unsuitable for medical applications, which require a good recognition rate.

A segmentation of retinal images into irregular shaped primary regions is performed in [6]. After a merging step remaining region bounds are considered to be vessels. Besides the use of noise-sensitive differentiating operators it remains unclear whether this method is well suited for the recognition of vessels with given characteristics stated above.

Tracking methods are known as the most powerful vessel recognition methodology [2,7], because vessel properties like local continuities and connectivity [2] can be carefully modeled. By combining tracking with matched filters the local vessel shape can be included into the model and the algorithm becomes more robust against noise. Due to extensive use of the a-priori knowledge about vessel structures, tracking methods show good results. However, the quality of the matched filters depends largely on the accuracy of signal and noise models, which has not been investigated sufficiently so far. This problem is addressed in section 2 and a precise vascular filter is derived from the angiographic imaging acquisition process.

¹ The large amount of noise comes from the image acquisition process, where two angiograms are subtracted from each other.

Modeling of local vessel continuities can be improved using an explicit vessel model. This task is investigated by applying an optimizing Kalman filter in section 3. This is the most consistent solution of the mentioned tracking process and permits an optimization of some heuristic tracking parameters.

The main result presented in this article is an automated structural check of the detected vasculature which has not been investigated so far. Although evaluation is of prime importance in medical applications, in many published techniques the problem remains unsolved [8]. Other approaches use manual benchmarks [2,7] or synthetic images [5,9] to verify their results. In section 4, this is automated by postulating structural assumptions for vessels and evaluating them afterwards. Results are discussed and conclusions are drawn in section 5 and 6. Further details can be found in [10].

2 Vascular Matched Filters

Matched Filters are optimum filters for the detection of a known signal in a noisy environment. In order to derive filter characteristics one has to investigate how vessels map to their corresponding signal in the image. This mapping happens due to attenuation of an X-ray beam, which integrates both vessel *and back tissue* attenuation contributions. Hence, back tissue may have a huge non-neglectable influence on the vessel signal. Due to this uncertainty the vessel signal is rawly approximated as Gaussian function [8] or assumed to have a rectangular shape [5,2]. However, the influence of the back tissue is eliminated in digital subtraction angiograms (DSA) by a subtraction of two logarithmized angiograms from each other. Furtheron, a linear map from vessel thickness to image intensity can be obtained. This permits the derivation of an accurate vascular filter: Assuming vessels as elliptical cylinders, each cross section is elliptic (except cuts along the medial axis). As shown in [11] all 1D densitometric profiles of the 2D elliptic cross section are half-elliptic (see figure 2a). Using this knowledge one can derive matched vessel filters modelling a small straight vessel section as half of an elliptical cylinder. Since we do not know diameter and direction of the vasculature, several matched filters $\text{mf}_{w,\theta}$ for a set \mathbb{W} of discrete widths and a set Θ of discrete orientations are applied. One of the filters in this set is depicted in figure 2b. The maximum convolution result r supplies both, an estimation whether each pixel $\text{image}(\mathbf{x})$ belongs to a vessel and its diameter and orientation (w^*, θ^*) . The filters are normalized in order to be invariant with respect to mean brightness and contrast; the latter was necessary to detect also tiny low contrast vessels. This results in $\forall \mathbf{x} : |r(\mathbf{x})| \leq 1$.

$$\begin{aligned} r(\mathbf{x}) &= \max_{(w,\theta) \in \mathbb{W} \times \Theta} \text{mf}_{w,\theta} * \text{image}(\mathbf{x}) \\ (w^*, \theta^*)(\mathbf{x}) &= \arg \max_{(w,\theta) \in \mathbb{W} \times \Theta} \text{mf}_{w,\theta} * \text{image}(\mathbf{x}) \end{aligned} \quad (1)$$

Obviously the elliptic assumption used above is not valid at branch points, crossings and stenoses with star-like shape. At these points the matched filter

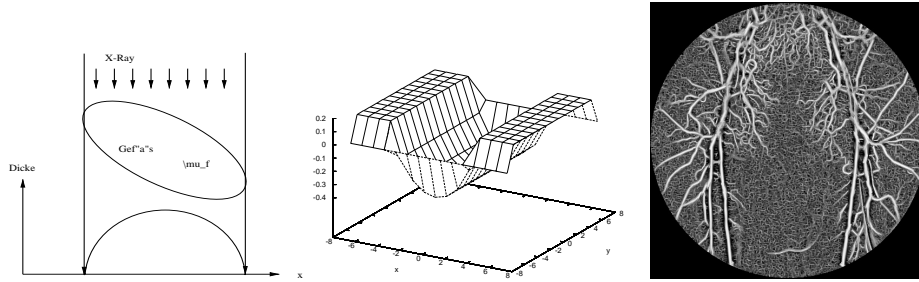


Fig. 2. a) Densitometric Profile b) Matched Vessel Filter c) Matched Filter Result

fails and additional efforts have to be undertaken at the tracking step to correct this filter malfunction.

The half-elliptic cylinder-shaped filter (see figure 2a) has a size of 13×13 pixels (best regarding to experiments). It is implemented for eight distinct orientations and for seven diameters of $\{1.0, 1.4, 1.9, 2.6, 3.5, 4.8, 6.5\}$ pixels. Figure 2c shows the maximum matched filter result of the DSA image in figure 1 over all possible orientations and diameters at each position, where the maximum matched filter result is mapped white.

3 Kalman Tracking

Tracking is used to model the local continuities of vessel properties and the vascular connectivity. Given a starting point and direction, the next point \mathbf{x}_n is estimated as the best among a set of possible vessel continuations [2]. This methodology can be improved using a Kalman filter, which has not been investigated in vessel tracking so far. The improvement is gained by using an *explicit* vessel model which allows a better modeling of anatomical knowledge of blood vessels and increases robustness. Here, a simple model is proposed by postulating a constant direction $(\Delta x, \Delta y)^T$ which is continued by a small step size $\delta_k \in \mathbb{R}^+$ during state transition. The state \mathbf{x}_k represents the current vessel position and direction. Due to the possibility to measure these variables directly by means of matched filters, the measurement map \mathbf{C}_k is Id , whereas state transition \mathbf{A}_k is given as

$$\mathbf{x}_k = \begin{pmatrix} x_k \\ y_k \\ \Delta x_k \\ \Delta y_k \end{pmatrix} \quad \mathbf{A}_k = \begin{pmatrix} 1 & 0 & \delta_k & 0 \\ 0 & 1 & 0 & \delta_k \\ 0 & 0 & 1 & 0 \\ 0 & 0 & 0 & 1 \end{pmatrix}.$$

In a small 3×3 neighborhood NB is searched for the maximum of the matched filter output and y^* is accepted as the measurement \mathbf{y}_m if r^* is larger than a certain threshold value $t_{min} = 0.67$.

$$r^* = \max_{\mathbf{y} \in NB} r(\mathbf{y}) \quad y^* = \arg \max_{\mathbf{y} \in NB} r(\mathbf{y})$$

If $r^* \leq t_{min}$ the step size δ_k is increased and the estimation step is carried out again until a valid \mathbf{y}_m is found or the iteration limit $l = 3$ is reached. By this methodology small vessel gaps are skipped which may be caused by stenotic lesions and a malfunction of matched filters (see section 2). If $r^* > t_{min}$ the state is updated with the accepted measurement and step size δ_k is reset to its initial value $\delta_0 = 1$.

Obviously, this procedure does not model junctions, the tracking process rather follows the vessel branch providing the strongest signal. For conventional tracking this problem is investigated by recursively detecting branch points along both vessel edges by use of matched filters [7] and tracking them. This approach was applied here also, where a branch is assumed if r^* is larger than a certain threshold value t_{junc} . Only vessel sections connected with the starting point are found. This drawback can lead to the missing of whole vessel section if a stenotic lesion stops the tracking at some point before. This problem can be solved by choosing several starting points $\{\mathbf{s}\}$ as $\{\mathbf{s}\} = \{\mathbf{s}, r(\mathbf{s}) > t_{seed}\}$ with $t_{seed} = 0.82$. Clearly this method does not ensure that a starting point is located in each connected component, but it is more robust than just using one starting point. Small vessels can be in $\{\mathbf{s}\}$ as well, since the matched filter only measures the similarity of the image signal to a half-elliptical cylinder, but not the contrast. Due to multiple starting points, the tracking result does not have to be a one pixel wide line, thus a thinning algorithm is applied. To compare Kalman tracking

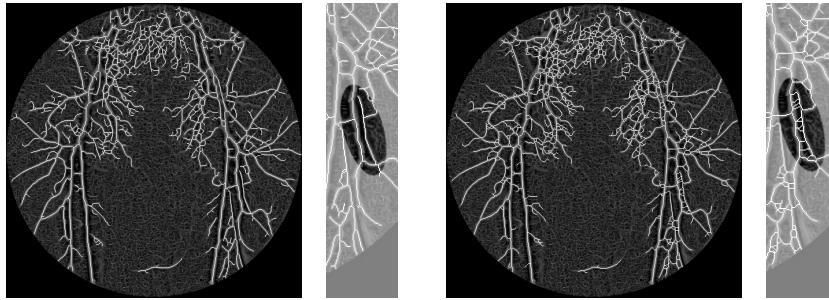


Fig. 3. a) Kalman Tracking b) Conventional tracking similar to [2]

to common tracking algorithms [2], both methods have been applied to DSA images as depicted in figure 1. For illustration purposes, the Kalman tracking graph and the conventional tracking are overlayed to the matched filter results, as shown in figure 3. The test shows better performance of the Kalman Filter in comparison to the conventional tracking, where many non-existent small vessels were detected – compare closeups (right images) of figure 3a and 3b.

4 Structural Check

We use a structural property \mathfrak{A} about vessels and check the segmentation result of section 3 using this property. \mathfrak{A} reads as follows: The original vessel in 3D

contains only nodes of degree ≤ 3 . By means of a medical vessel catalogue one verifies that \mathfrak{A} applies to the overwhelming majority of branch points [12].

We define \mathbb{S} as the set of abstract graphs for which \mathfrak{A} holds. Let P be the projection of an abstract 3D-embedded graph to an abstract graph embedded in 2D. Thus the question of structural evaluation arises: *Given a graph \tilde{g} obtained from vectorizing the tracking result, can one element of \mathbb{S} be an admissible origin of \tilde{g} with regard to projection P ?* If this question can be affirmed, the structural test is passed. Otherwise, which modifications are to be applied to graph \tilde{g} to ensure that \tilde{g} is in the $\text{Range}(P) = P(\mathbb{S}) = \{P(s) : s \in \mathbb{S}\}$?

Let g be a realization of an abstract graph embedded in 3D. Then the projection P is presented considering the following cases:

- I. $P(g)$ is isomorphic to g . This is depicted as $P_1(g)$ in figure 4.
- II. Two nodes of g are mapped onto each other and glued, thus $P(g)$ contains one node less than g . This is illustrated as $P_2(g)$ in figure 4 by $n_4 \mapsto n_3$.
- III. A node of g is mapped to a point $p(e^2)$ of an edge e^2 of g , this splits e^2 into two subedges e_1 and e_2 . This is shown as $P_3(g)$ in figure 4 by $n_4 \mapsto p(e^2)$.
- IV. A point an edge e^1 of g is mapped to a point of another edge e^2 of g , this splits e^1 and e^2 into two subedges in each case and creates a new node n_5 at the edge crossing – depicted as $P_4(g)$ in figure 4 by $p(e^1) \mapsto p(e^2)$.

The Projection P is modeled as a finite composition of N specific projections $\{P_2, P_3, P_4\}$. Each P_i maps *distinct* nodes and edges of the graph. P_1 is omitted because it does not change the graph structure.

$$P(g) = P_{a(1)} \circ \dots \circ P_{a(N)}(g) \quad \forall i : a(i) \in [2, 4] \quad (2)$$

Let \mathbb{K} be the set of nodes of degree ≥ 4 in $P(g)$. If there exists a node $n \in \mathbb{K}$, then it must have resulted from the projections P_2, P_3, P_4 , because there is no node with degree ≥ 4 in g according to property \mathfrak{A} . With each of these projections P_i a cycle results from glueing together formerly disjoint pairs of edges or nodes, if g is connected. This cycle results in a face, if not all cycle edges are projected onto each other. Thus, if there exists a node $n \in \mathbb{K}$, then it is a “point of glueing” and incident to a face. Therefore each node $n \in \mathbb{K}$ can be mapped by a bijection \mathbf{i} to the face f which is generated by the same glueing like n . Let \mathbb{F}_g the set of faces in $P(g)$ generated by this glueing, then the bijection $b : \mathbb{K} \rightarrow \mathbb{F}_g$ is to be determined.

Let \mathbb{F} be the set of faces in $P(g)$, then the problem can be represented using a bipartite graph G with bipartition \mathbb{K} and \mathbb{F} . The graph edges $(n, f) \in \mathbb{K} \times \mathbb{F}$ symbolize that node n is incident to face f . Next the task of determining bijection \mathbf{i} which can be reformulated in terms of maximum cardinality *matching*, which is a maximum cardinality edge subset of G such that no two of them share a node in common, i.e. see figure 5. The maximum matching problem solved by the theorem of König and Hall [13], which provides an algorithm finding this matching M in polynomial time $O(|\text{nodes}(G)| |\text{edges}(G)|)$. If the match algorithm succeeds, we can assign a distinct face to every node $n \in \mathbb{K}$ and the structural test is passed. If the test fails, we receive a “failure set” k which can be used for

error correction. Type of error correction depends on the intended applications of this vessel segmentation:

Content-orientated image compression: For each node n in k , additional edges incident to n are searched, since additional vasculature lowers compression ratio, but missing components may cause the uselessness of the compressed image for diagnosis.

Diagnosis support: We mark \mathbb{S} as uncertain and show the result to the user. Hence, the automated error correction only produces suggestions for user interaction, because diagnosis is inherently interactive.

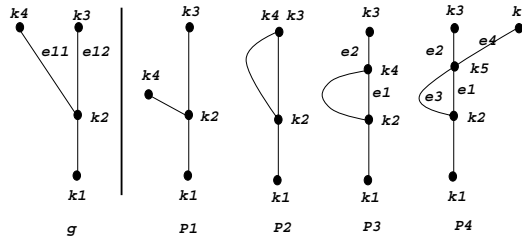


Fig. 4. Map P from 3D to 2D image plane

Passing this test is a necessary but not sufficient condition for ensuring that the detected graph \tilde{g} is in the $\text{Range}(P)$. Sufficiency can be achieved by applying all P_i^{-1} in inverse order to \tilde{g}

$$\hat{g} = P_{a(N)}^{-1} \circ \dots \circ P_{a(1)}^{-1}(\tilde{g}) \quad \forall i : a(i) \in [2, 4] \quad (3)$$

and checking whether $\hat{g} \in \mathbb{S}$ is true. Any $P_{a(i)}^{-1}$ means to split the node n which was glued by $P_{a(i)}$, whereby the connectivity is preserved by the face $\mathbf{i}(n)$. Due to the enormous variety of possible application sequences of the $P_{a(i)}^{-1}$ in (3) this is too time-consuming and has not been applied.

The graph theory part is implemented using the LEDA C++ library [14]. A sample matching is shown in figure 5, where nodes of degree ≥ 4 form the left column and faces the right column. The bold edges represent the matching, which covers all nodes of the left column. Thus, no error correction step is necessary.

5 Experimental Results

The main experimental problem is to get the true segmentation of vasculature in DSA images, since manual segmentation is very time-consuming. Furtheron, a statistically significant amount of manual segmentations to measure segmentation accuracy as consistency between different segmentations and different segmenters. Finally, an accurate segmentation of line-like structures is impossible on pixel scale, since tiny vessel arcs cannot be approximated properly by manual

drawn polygons. Hence, as a matter of principle manually segmented line-like structures are not very reliable. Thus, synthetic images are favored here, because they do not possess the mentioned disadvantages. However, synthetic images never model all details of “real world” images, so a few manual segmentations are still included into the test set.

The image generation process and noise contributions are well known for DSA images (see chapter 2 and [15]). This enables the possibility to generate precise synthetic images using the stochastic generated vessel tree. Given a user-supplied initial vessel section the next one is estimated as Gaussian distributed random variable around the initial direction. The branching probability is proportional the ratio of unbifurcated vessel length and vessel diameter.

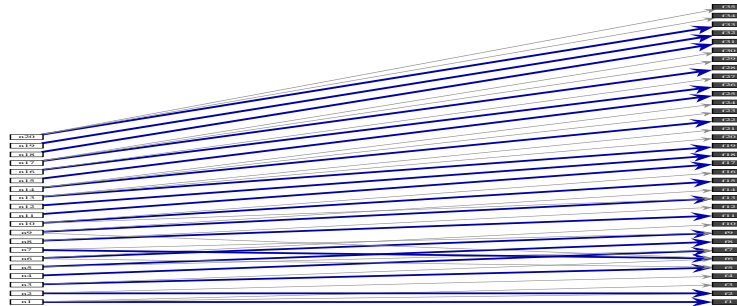


Fig. 5. Sample Maximum Cardinality Matching

Next, we introduce sensitivity/specificity as the probability to classify an object/background pixel correctly. The average of both probabilities serves as the objective function f for the optimization of heuristic tracking parameters. These parameters are t_{min} (tracking continuation), t_{seed} (starting points) and t_{junc} (branch points) as described in section 3. These parameters control the tracking process with respect to the maximum matched filter result (1), which is a measure of vessel similarity. The presence of vessels on a noisy background can be assumed for $r \in [0.5, 0.9]$. Hence, we choose an $(t_{min}, t_{junc}, t_{seed}) \in [0.4, 1]^3$ as optimization domain. For a test set of 20 synthetic and two “real” images all results were averaged. Objective function, sensitivity and specificity as function of (t_{min}, t_{junc}) are shown in figure 6, where the remaining parameter is set to its optimal value $t_{seed} = 0.82$. For small values of t_{min} and t_{junc} a lot of pixels are selected for tracking. Hence, sensitivity is high and specificity low. With increasing t_{min} and t_{junc} less pixels are assumed to be vasculature resulting in decreasing sensitivity and increasing specificity. We obtain the maximum of the objective function $\max(f) = 0.98$ at $(t_{min}, t_{junc}, t_{seed}) = (0.63, 0.82, 0.82)$, which corresponds to an average sensitivity of 0.97 and an average specificity of 0.98. Segmentation results of “real” and synthetic images are shown in figure ??, where black/white pixels are correctly classified object/background pixels. Gray pixels are misclassified object or background pixels. We obtain a sensitivity/specificity of 0.85/0.92 for figure ??a whereas values are higher (0.98/0.99) for figure ??b. There are two reasons, why synthetic images provided much bet-

ter results: At first, synthetic images don't model all details of "real world" images. We obtain this effect in comparison with a "real" DSA image in figure 1, where some vessel overlays (upper left) are much more complicated. Secondly, the manual segmentation is not very reliable and labeling *all* tiny vessel is too time-consuming and therefore almost impossible, i.e. a lot of tiny vessels in the middle of the upper half of figure 1 are not labeled yet. The true sensitivity is expected to be inbetween synthetic sensitivity and "real" data results.

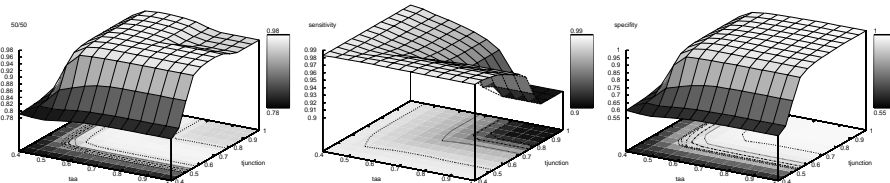


Fig. 6. Objective function f , sensitivity se and specificity sp , $t_{seed} = 0.82$

Next, we show the applicability of the structural check as described in section 4. An error of the vessel graph of figure 1 detected by the structural check is depicted in figure ??c: A node of degree ≥ 4 which cannot be mapped to an incident face. Obviously the check does not cover all structural errors, since some information is lost during projection in 2D. However, the check provides the detection of some false segmentations. Hence, the algorithm fits its purpose of checking segmentation. Experiments indicate, that detected errors are over-segmentations, where the tracking starts to follow non-real vessels.

6 Conclusion

A new method for automated vessel segmentation is proposed. The first improvement with respect to conventional approaches is the derivation of an accurate matched vascular filter from the angiographic acquisition process. Imaging equations are considered as well as the noise spectrum. Next, the exploitation of anatomical knowledge about blood vessels in the the tracking process is improved by applying an optimizing Kalman filter.

The main contribution to vessel segmentation is the automated check of the detected vasculature by means of testing necessary structural properties. If this test fails, locations of possible errors are supplied by the algorithm. Thus missing parts can be searched automatically or interactively and detection errors can be eliminated.

The new method shows very good results and an average sensitivity of 0.97 and an average specificity of 0.98. Even very small and hardly recognizable vessels have been detected. The structural evaluation enables the detection of some wrong segmentations. Experimental results indicate, that detected errors are mainly oversegmentations.

The developed segmentation is intended for semantic image compression. The gained information is used for the local adjustment of image quality. In

this context any violation of the structural property \mathfrak{A} would result in a slightly smaller compression ratio and can be neglected. The method can be used also for diagnosis support, if we ensure that assumption \mathfrak{A} applies to the examined body region.

References

1. Wong, S., Zaremba, L., Gooden, D., Huang, H.K.: Radiologic image compression. *Proceedings of the IEEE* **83** (1995) 194–218
2. Sun, Y.: Automated identification of vessel contours in coronary arteriograms by an adaptive tracking algorithm. *IEEE Trans. on Med. Imaging* **8** (1989) 78–88
3. Lindeberg, T.: Edge detection and ridge detection with automatic scale selection. In: *Proc. CVPR'96, San Francisco, California.* (1996)
4. Krissian, K., Malandain, G., Ayache, N.: Directional anisotropic diffusion applied to segmentation of vessels in 3D images. *Lecture Notes in Computer Science* **1252** (1997) 345 – 348
5. Kottke, D.P., Sun, Y.: Segmentation of coronary arteriograms by iterative ternary classification. *IEEE Trans. on Biomed. Eng.* **37** (1990) 778–785
6. Jasiobedzki, P., Taylor, C.J., Brunt, J.N.H.: Automated analysis of retinal images. *Image and vision computing* **11** (1993) 139–144
7. Liu, I., Sun, Y.: Recursive tracking of vascular networks in angiograms based on the detection-deletion scheme. *IEEE Trans. on Med. Imag.* **12** (1993) 335–341
8. Chaudhuri, S., Chatterjee, S., Katz, N., Nelson, M., Goldbaum, M.: Detection of blood vessels in retinal images using two-dimensional matched filters. *IEEE Trans. on Med. Imaging* **8** (1989) 263–269
9. Figueiredo, M.A.T., Leitaao, J.M.N.: A nonsmoothing approach to the estimation of vessel contours in angiograms. *IEEE Trans. on Med. Imaging* **14** (1995) 162–172
10. Franz, M.: *Semantische Kompression* (in German). PhD thesis, TU Dresden, Department of Computer Science, Artificial Intelligence Institute, Germany, Available at <http://www.iee.et.tu-dresden.de/~franz/cv.html> (2003)
11. Pellot, C., Herment, A., Sigelle, M., Horain, P., Maitre, H., Peronneau, P.: A 3D reconstruction of vascular structures from two x-ray angiograms using an adapted simulated annealing algorithm. *IEEE Trans. on Med. Imag.* **13** (1994) 48–60
12. Sobotta, J.: *Atlas of Human Anatomy.* Williams & Wilkins (1990)
13. West, D.B.: *Introduction to Graph Theory.* Prentice Hall (1995)
14. Mehlhorn, K., Näher, S., Seel, M., Urig, C.: LEDA C++ class library, version 3.8. Available at <http://www.mpi-sb.mpg.de/LEDA/> (1999)
15. de Bruijn, F.J., Slump, C.H.: Lossy cardiac X-ray image compression based on acquisition noise. *SPIE Proc.* **3031** (1997) 302–311